

Article

Pore Connectivity Characteristics and Controlling Factors for Black Shales in the Wufeng-Longmaxi Formation, Southeastern Sichuan Basin, China

Fei Zhao ^{1,2}, Zaitian Dong ^{2,*} , Chaoyong Wang ², Wenli Zhang ³ and Rui Yu ⁴¹ Xuzhou Datun Engineering Consulting Co., Ltd., Xuzhou 221618, China; zhaof8401@163.com² School of Resources and Earth Sciences, China University of Mining and Technology, Xuzhou 221008, China; wangcy@cumt.edu.cn³ School of Management, Xi'an University of Science and Technology, Xi'an 710054, China; 20302219038@stu.xust.edu.cn⁴ School of Mines, China University of Mining and Technology, Xuzhou 221008, China; TS10010014@cumt.edu.cn

* Correspondence: dongzt@cumt.edu.cn; Tel.: +86-180-3590-4290

Abstract: Investigations into the connectivity and complexity of pore systems in shales are essential for understanding the flow of shale gas and the capacities of the associated reservoirs. In the present study, eight shale samples from the Wufeng-Longmaxi (WF-LMX) Formation that were collected from Well Yucan-6 in the southeast of the Sichuan Basin were analyzed for microstructural, pore network, and pore connectivity characteristics. The measurement results of low-pressure nitrogen adsorption illustrated that all shale samples contain micropores, mesopores, and macropores. Micropores and mesopores account for a high proportion of the total pores, and the dominant pore throat size is in the range of 2–6 nm. High-pressure mercury injection tests reveal that the porosity, total pore volume, and total specific surface area of pores for samples from the WF Formation are higher than those for samples from the LMX Formation. In spontaneous absorption experiments, the slopes of the absorption curves of *n*-decane (oil-wetting) and deionized water (water-wetting) in the WF and LMX Formations varied from 0.254 to 0.428 and from 0.258 to 0.317, respectively. These results indicate that shales in both formations exhibit mixed wettability characteristics, but lipophilic pores are better connected relative to hydrophilic pores. The total organic carbon and silica contents are the main factors controlling the pore connectivity in these shales, while the effects of other minerals are not significant. The findings of this work can improve our understanding of the pore structure characteristics of black shale.

Keywords: pore size distribution; pore connectivity; marine shale; Wufeng–Longmaxi Formation; Sichuan Basin



Citation: Zhao, F.; Dong, Z.; Wang, C.; Zhang, W.; Yu, R. Pore Connectivity Characteristics and Controlling Factors for Black Shales in the Wufeng-Longmaxi Formation, Southeastern Sichuan Basin, China. *Energies* **2022**, *15*, 2909. <https://doi.org/10.3390/en15082909>

Academic Editors: Yuming Liu, Xixin Wang, Luxing Dou, Mofazzal Hossain and Reza Rezaee

Received: 24 February 2022

Accepted: 12 April 2022

Published: 15 April 2022

Publisher's Note: MDPI stays neutral with regard to jurisdictional claims in published maps and institutional affiliations.



Copyright: © 2022 by the authors. Licensee MDPI, Basel, Switzerland. This article is an open access article distributed under the terms and conditions of the Creative Commons Attribution (CC BY) license (<https://creativecommons.org/licenses/by/4.0/>).

1. Introduction

Owing to advances in fracturing and drilling technology, production of shale gas has substantially improved [1–4]. Shale gas occurs mostly in a free or adsorbed state in different types of pores or on the surface of mineral particles [5]. Shales rich in organic matter (OM) and clay minerals, also known as black shale, have pore characteristics closer to nanoscale than carbonate and sandstone [5–7]. Additionally, they are characterized by low porosity and low permeability. In shale gas exploitation, it is necessary to use hydraulic fracturing to produce artificial cracks in the rock to connect the nanoscale pores to meet the needs of industrial exploitation. Therefore, investigations of the structure and connectivity of pores in shales are valuable for understanding the development of the associated pore systems, and thus for improving our knowledge of the mechanisms of shale gas accumulation.

The organic matter-rich shales of the Wufeng-Longmaxi (WF-LMX) Formation are assigned to the Late Ordovician–Early Silurian ages. These shales, which are widely

distributed in the Sichuan Basin and its environments, constitute an important stratum for the production of marine shale gas in China [7]. Many studies have been conducted on the structure of pores in shales and their connectivity. The lattice Boltzmann method (LBM), for example, has been utilized to quantitatively characterize the pore structures of and diffusion in organic matter-rich shales [8–10]. Nuclear magnetic resonance (NMR) has been employed to qualitatively characterize pore and fluid types in organic matter-rich shales [11,12]. Dielectric dispersion log interpretation has also been used to discuss the formation evaluation in unconventional formation [13–16]. Additionally, X-ray micro- or nano-computed tomography (X-ray CT) and scanning electron microscopy (SEM) have been applied to evaluate the three-dimensional (3D) connectivity of pores in organic matter-rich shales [17–19]. Further, high-pressure Hg intrusion porosimetry (MICP), low-pressure CO₂ and N₂ adsorption, small- and ultrasmall-angle neutron scattering, and helium porosity measurements have been commonly used to study pore characteristics in shales [19]. The connectivity of shale pores can also be evaluated by studying the porosity differences determined by small-angle neutron scattering, mercury injection capillary pressure and the helium-specific gravity method [20–22]. A nanotransmission X-ray microscope, a focused ion beam scanning electron microscope, and other equipment are also used to reconstruct 3D pore networks [23,24]. As another simple and effective method, spontaneous imbibition is widely used to characterize the connectivity between shale pores [25]. The above studies also found that the differences of imbibition materials and shale mineral composition have a significant impact on the imbibition results.

However, studies on the characteristics of pore connectivity and controlling factors in organic-rich shales are mostly qualitative or quantitative. Therefore, further studies integrating qualitative and quantitative analyses are required. The purpose of this work is to study the control factors of shale pore connectivity (e.g., pore types, pore size distribution, and wettability). The results of low-pressure N₂ adsorption, MICP, and X-ray were compared and discussed of overmature shale samples, and the differences in the spontaneous absorption of deionized water and n-alkane were supplemented. The findings of the present study can improve our understanding of the pore structure characteristics of black shales and the related shale gas accumulation.

2. Geological Setting

The Sichuan Basin is an NNE-trending rhombus-shaped basin in the northwestern margin of the Yangtze Platform, and is surrounded by mountains (Figure 1a). Starting during the period from the Paleozoic to the Cenozoic, the Sichuan Basin evolved from a craton to a foreland basin through diverse processes, and then to a superimposed marine-continental basin [26]. From Late Ordovician to Early Silurian, two global transgressions produced low-energy and anoxic environments across the basin, and black shales of the WF-LMX were deposited [27] (Figure 1b).

Well Yucan-6 (29°042.8' N and 108°581.2' E) was located in the southeast of the Sichuan Basin in the southeast of Chongqing, Youyang County, China, and the WF-LMX Formation was entirely traversed in this well (Figure 1c). The lithology of the LMX Formation comprises brown-gray argillaceous shales, black-gray carbonaceous shales, and brown-gray silty shales, and these occur at depths ranging from 679.05 to 774.29 m. This formation is underlain by the WF Formation and overlain by the Xintan Formation. The WF Formation comprises black-gray carbonaceous silty shale containing graptolites, and these occur at depths of 774.29–781.75 m. This formation is underlain by the Linxiang Formation and overlain by the LMX Formation.

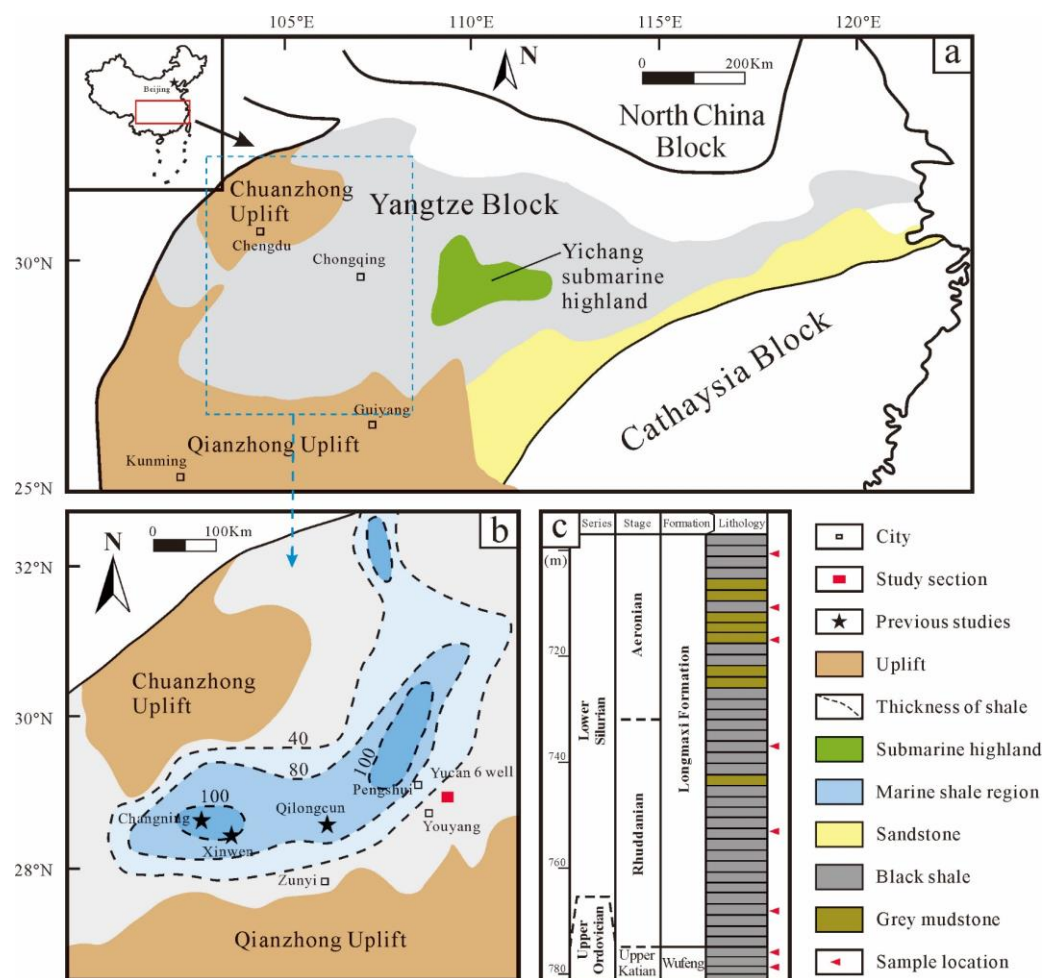


Figure 1. Ancient geographical location of the study well. (a) Geographical location of the Sichuan Basin in South China (adopted from [26]); (b) locations of Well Yucan-6 and related sections during the Early Silurian stage (adapted from [27]); (c) a stratigraphic column based on the Yucan-6 well.

3. Samples and Methods

3.1. Samples

In this work, eight fresh and representative shale samples were collected from Well Yucan-6. These included two samples from the WF Formation and six samples from the LMX Formation. The location of the well and the associated information on the collection of samples are demonstrated in Figure 1b,c, respectively. All the samples were directly obtained from cores without any treatment. Total organic carbon (TOC), mineral composition, low-pressure N_2 adsorption, and high-pressure MICP analyses, in addition to spontaneous absorption experiments, were performed for all the samples. In addition, the 3D pore characteristics of one sample from each formation were investigated by X-ray analysis.

3.2. Methods

The procedures utilized for the measurement of the TOC and mineral composition have previously been reported in detail [28]. Prior to the low-pressure N_2 adsorption measurements, samples were ground to sizes of 60–80 mesh, then dried under vacuum for 48 h at 383 K, followed by the analysis of the samples using a Micromeritics ASAP 2020 analyzer. The Brunauer–Emmett–Teller (BET) and density functional theory (DFT) models were used to calculate the specific surface areas and pore volumes of the shale samples, respectively [29,30]. To describe and quantify the pore structure and complex surface information of irregular porous media, the fractal dimension of the shale samples was calculated using the Frenkel–Halsey–Hill (FHH) model [31].

MICP measurements were performed on irregular blocks of samples measuring 2–5 mm in diameter using an AutoPore IV 9510 mercury porosimeter (Micromeritics Inc., Atlanta, GA, USA). Pores or capillaries were assumed to be cylindrical with circular cross-sectional openings, and the Washburn equation was used to calculate pore throat sizes [32]. The value utilized for the surface tension was 485 dyne/cm, while the contact angle for Hg was 140°. An injection pressure of 0.1 MPa was used as a standard for the calculations, while the method proposed by Peng et al. [33] was employed for the correction of the MICP data. The difference between the volumes of Hg injected was based on the pressure, and that associated with the standard for the calculation was the final cumulative volume of Hg injected, and the influence of compression was neglected.

During the spontaneous absorption experiments, cylindrical plugs of shale samples measuring approximately 20 mm in height were prepared, then coated with epoxy resin to reduce fluid adsorption and evaporation, except at both ends. The samples were placed in an oven at 60 °C for 48 h before the experiments, and the temperature during the experiments was 23 °C. Changes in the weight of samples versus time were automatically recorded as the absorption proceeded using a high-precision electronic balance. The fluids used for the absorption experiments were deionized water and *n*-decane.

The X-ray scanning tests were performed on samples using a MicroXCT-200 CT scanner (ZEISS Xradia, Minneapolis, MN, USA). The equipment involves a 150 kV/15 W high power focus X-ray tube, and the maximum resolution is 1.0 µm. Cylindrical core samples were mounted in the vertical position onto the sample holder to ensure a central field of view for the scanner, and each sample was then scanned using a conical ion beam emitted from the X-ray source. The X-ray intensity was attenuated as it passed through the sample, and these signals were recorded by the detector. The samples were rotated and scanned at different angles until 360° scanning was achieved.

4. Results

4.1. TOC Content and Mineral Composition

The TOC content of the samples ranged from 1.01 wt.% to 4.79 wt.% (mean = 1.99 wt.%). Compared to samples from the LMX Formation (average = 1.13 wt.%), the TOC contents for samples from the WF Formation presented in Table 1 were higher (average = 4.57 wt.%) than those from the LMX Formation.

Table 1. TOC contents and basic mineral composition data for shales from the WF-LMX Formation.

Formation	Longmaxi Formation						Wufeng Formation	
Samples	Yc01	Yc02	Yc03	Yc04	Yc05	Yc06	Yc07	Yc08
Depth (m)	710.8	715.4	718.3	734.6	753.7	768.3	773.3	775.4
TOC (wt.%)	1.03	1.15	1.01	1.3	1.16	1.13	4.34	4.79
Silica (%)	39.9	41.2	37.2	46.3	38.4	40.1	48.1	46.3
K-feldspar (%)	7	5.4	7.4	3.6	5.1	7.9	6.8	1.2
Plagioclase (%)	15.9	9.5	20.7	5.4	20.4	18.9	13.1	9.4
Calcite (%)	8.6	1.6	7.5	1.3	3.8	5.4	2.1	8.7
Dolomite (%)	9	1.5	5.3	1.4	11.1	8.8	8.6	5.9
Pyrite (%)	2	4.8	1.5	3.2	1.6	1.9	-	7.3
Clay mineral (%)	15.8	28.3	17.5	36.5	17.2	14.1	14.3	13.9

Quartz and clay minerals accounted for more than 50% of the minerals in the shale samples (54.7–74.5%, with an average of 60.85%), while calcite varied from 1.3% to 8.7% (mean = 4.88%), and other minerals occurred in subordinate proportions. However, the quartz contents of samples increased with depth, while the clay mineral contents decreased (Table 1 and Figure 2). Sample Yc07, which was obtained from a depth of 773.3 m, produced the highest quartz content of 48.1%, followed by 46.3% for sample Yc08, which was collected from a depth of 775.4 m (Table 1). According to previous studies, quartz in shales of the WF-LMX Formation is mainly biogenic, and this indicates that a high paleoproductivity is

conductive to the preservation of large amounts of OM [28,34]. A high quartz content also increases the brittleness of shales, and this is beneficial for the production of shale gas.

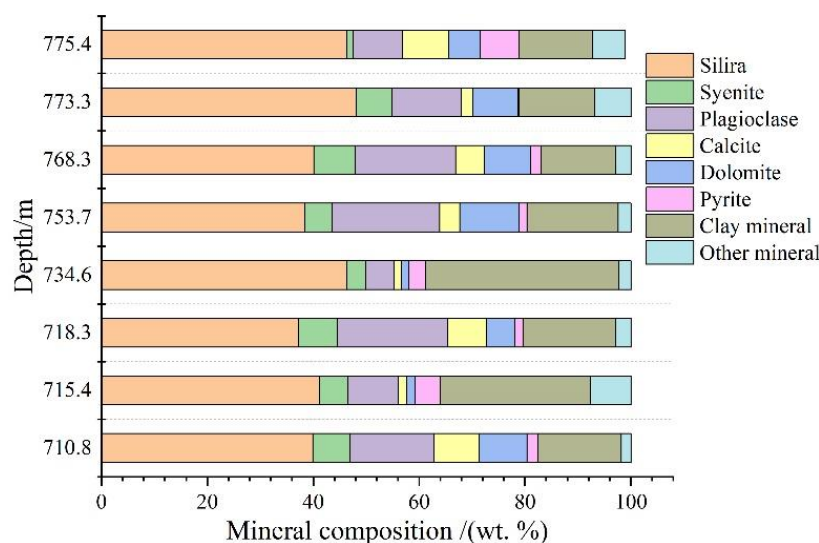


Figure 2. Diagram illustrating the mineral composition of shale samples studied according to depths.

4.2. Pore Size Distribution

Low-pressure N_2 adsorption and MICP are effective methods for measuring pore volumes and characterizing types of pores in porous media [35]. The characteristics of samples from the WF-LMX Formation during N_2 adsorption and MICP measurements are displayed in Figures 3 and 4, respectively, and the associated pore size distribution data are presented in Table 2.

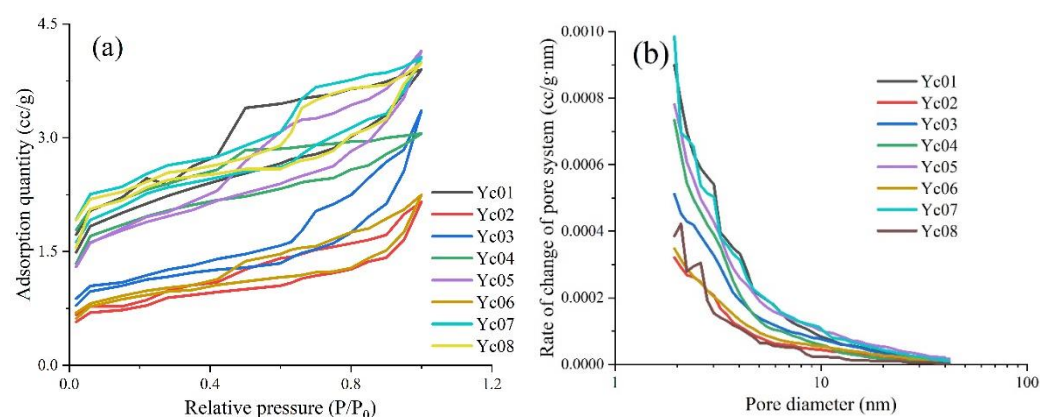


Figure 3. Plots illustrating (a) the low pressure N_2 adsorption–desorption responses of the shales studied and (b) the pore size distribution of the samples.

Evidently, the low-pressure N_2 adsorption–desorption characteristics of the shales from the WF-LMX Formation were similar. In the low relative pressure section ($P/P_0 < 0.40$), the adsorption was obvious, while in the intermediate relative pressure section ($0.4 < P/P_0 < 0.9$), a hysteresis loop associated with the adsorption–desorption was evident for the samples. However, in the high relative pressure section ($P/P_0 > 0.9$), a significant upward trend was observed for the samples (Figure 3a). The N_2 adsorption isotherms of the eight samples were generally inverse ‘S’ type, which is closest to type IV with adsorption steps in the IUPAC isothermal adsorption line classification standard [36]. The overall shape of the hysteresis loops was similar, but the degree of development was different. The higher the TOC content, the greater the hysteresis loop. According to the classification of hysteresis by IUPAC, the pore types of shale samples in the LMX Formation were mainly tabular pores,

and the shale samples in the WF Formation were mainly cylindrical and inkbottle pores. Furthermore, the low-pressure N_2 adsorption isotherms of the samples revealed that the shale samples from the WF-LMX Formation contained micropores (<2 nm), mesopores (2–50 nm), and macropores (>50 nm).

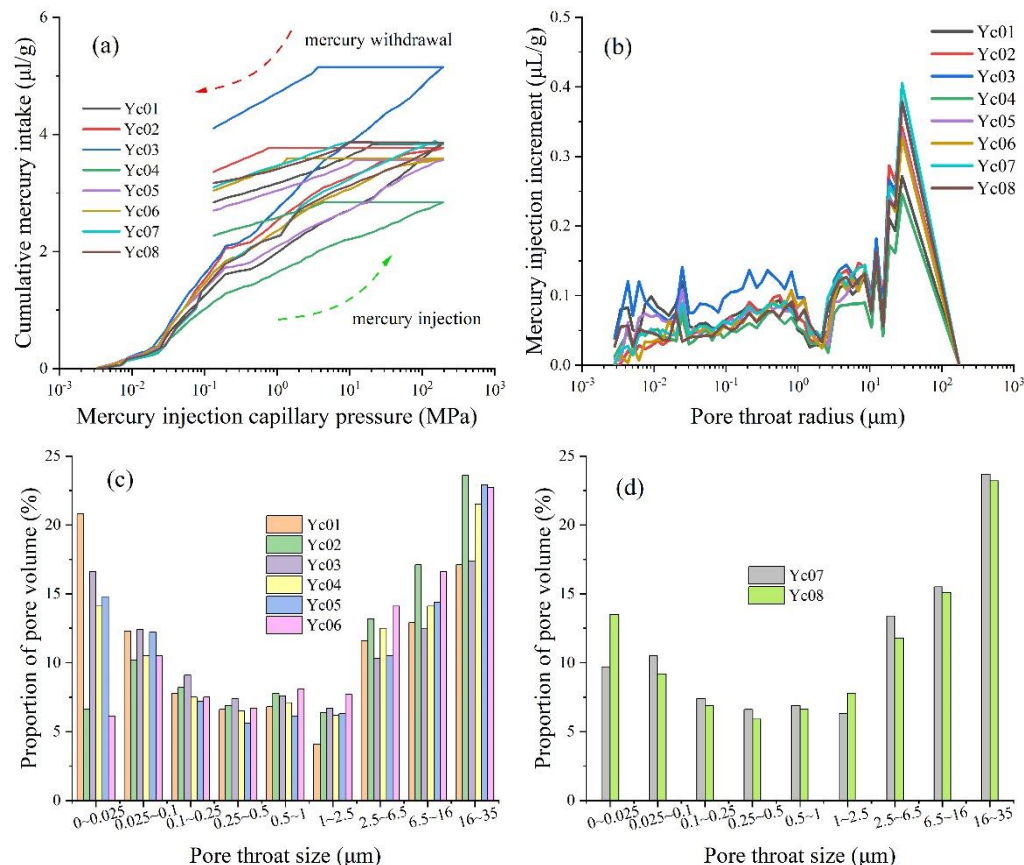


Figure 4. Plots illustrating (a) the high-pressure mercury injection responses, (b) pore throat radius and (c,d) pore size distribution ranges for shales from the WF-LMX Formation.

The pore structure parameters of the shales were calculated and analyzed using the BET and DFT models, and the data are presented in Table 2. The specific surface areas of samples from the WF Formation varied from 7.47 to 7.72 m²/g (mean = 7.60 m²/g), while the average pore throat sizes ranged from 4.76 to 5.58 nm, and the total pore volumes were between 0.0039 and 0.0054 cm³/g (mean = 0.00465 cm³/g). Regarding samples from the LMX Formation, the specific surface area values ranged from 2.78 to 7.00 m²/g (mean = 5.54 m²/g), while the average pore size varied from 4.9 to 8.21 nm, and the total pore volume was between 0.0026 and 0.0047 cm³/g (mean = 0.00327 cm³/g). The distribution of the rate of pore volume changes illustrated that pores with sizes of 2–6 nm were dominant in samples from the WF-LMX Formation (Figure 3b). In the study of the total pore volume and specific surface area, it was found that mesoporous and macropores have the largest contribution to the total pore volume of shale, and micropores have the smallest contribution. However, the contribution of micropores to the pore specific surface area is larger, followed by mesopores; macropores can be ignored [37]. The smaller the pore, the larger the specific surface area.

The shape of the MICP curve reflects the pore throat size distribution and connectivity in a sample. The MICP curves of the samples studied were similar, and exhibited obvious hysteresis. This indicates that substantial amounts of Hg remained in the sample after the injection ended (Figure 4a); that is, a large pore volume (inkbottle effect) was present in each sample. The volume of Hg injected into samples from the WF Formation under maximum pressure varied from 3.88 to 3.89 μL/g, which is comparable to samples from the

LMX Formation (2.83–5.11 $\mu\text{L/g}$). These results indicate that pore development processes in shales of the LMX and WF Formation were similar.

Table 2. Data for parameters associated with pores in shale samples obtained from N_2 adsorption and MICP measurements.

	Formation	Longmaxi					Wufeng		
		Yc01	Yc02	Yc03	Yc04	Yc05	Yc06	Yc07	Yc08
N ₂ adsorption pore size distribution parameters	BET specific surface area (m ² /g)	3.94	6.96	2.78	7.00	6.37	6.20	7.47	7.72
	Micro-pores specific surface area (m ² /g)	3.04	5.44	2.15	5.78	5.36	5.33	6.21	6.46
	Average pore size (nm)	5.49	7.86	8.21	4.90	6.81	7.89	4.76	5.58
	Fractal dimension (D1 + D2)	5.2669	5.337	5.2435	5.4989	5.3869	5.277	5.0393	4.9794
	Total pore volume (cm ³ /g)	0.0027	0.0026	0.0043	0.0026	0.0047	0.0027	0.0039	0.0054
MICP pore size distribution parameters	Rock sample density (g/cm ³)	2.2	2.15	2.14	2.17	2.16	2.17	2.16	2.15
	Porosity (%)	1.61	1.62	2.2	1.22	1.55	1.77	2.03	1.84
	Total pore volume (cm ³ /g)	0.0073	0.0076	0.0103	0.0057	0.0072	0.0081	0.0094	0.0085
	Total specific surface area (m ² /g)	0.86	0.26	0.93	0.45	0.52	0.21	0.39	0.58
	Average radius (μm)	3.24	4.05	3.06	3.52	3.72	3.45	3.31	3.6

Data for the pore structure parameters obtained from the MICP measurements are presented in Table 2. In samples from the LMX Formation, the distributions of pore throat diameters greater than 20 nm were characterized by multiple peaks (Figure 4b,c), while those of the WF Formation had just one peak (Figure 4b,d). In the LMX samples, pores with throat radii of less than 0.1 μm and between 2.5 and 35.0 μm represented approximately 25% and 50% of the total pore volume, respectively. In contrast, the total pore volume in approximately 50% of samples from the WF Formation was accounted for by pores with throat radii of 2.5–35.0 μm (Figure 4d).

Evidently, there was a certain difference in the pore size distributions obtained by low-pressure N_2 adsorption and MICP. The reason for these differences is not only the heterogeneity of shale itself, but is also the specific pore space information provided by the above two test methods. MICP focuses on the measurement of pore throat size, while low-pressure N_2 adsorption evaluates the distribution of pore size [15].

4.3. Connectivity of Pores

The responses from the spontaneous absorption of *n*-decane and deionized water for the samples are displayed in Figures 5 and 6, respectively. The fluid imbibition experiment is the process of the wetting phase spontaneously displacing the nonwetting phase under capillary pressure. The slope of the self-absorption curve is always used to evaluate pore connectivity characteristics. Evidently, during the initial stage, the absorption increased rapidly as the time increased (logarithmic coordinates). The fluctuations in the curves for various samples were caused by the boundary effects of the contacts with fluids [38]. After the initial stage, the absorption increased steadily with time, and the slopes were quite different (Figures 5 and 6). Slopes for the absorption of *n*-decane in the shales of the WF and LMX Formations ranged from 0.415 to 0.428 and 0.254 to 0.406, respectively, while those for deionized water were correspondingly 0.298–0.315 and 0.258–0.317 (Table 3). The results of the absorption experiments suggest that pores in the shales are slightly more lipophilic than hydrophilic.

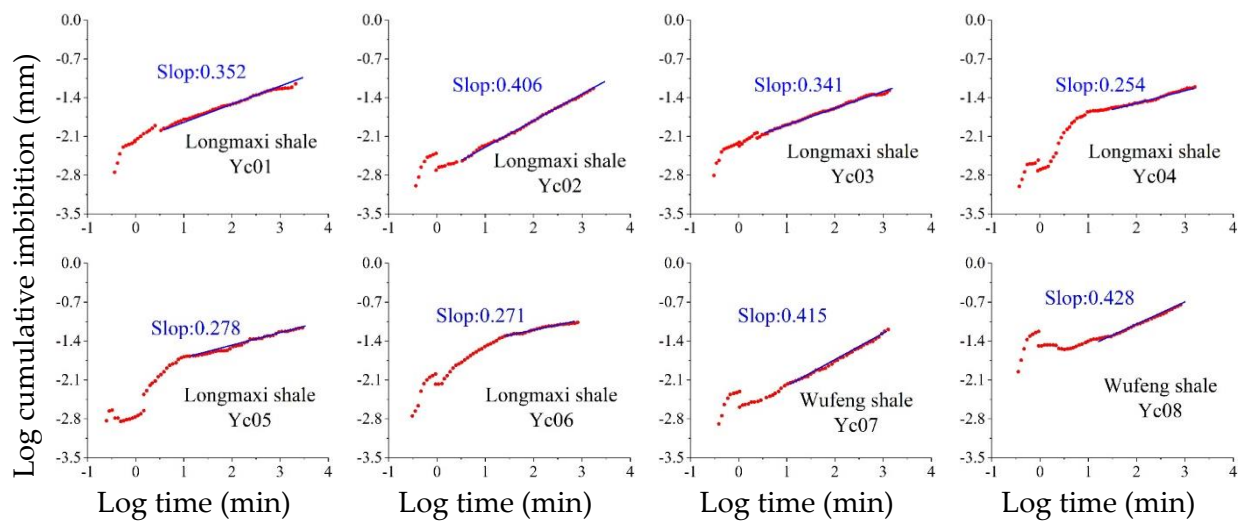


Figure 5. Log plot of the cumulative imbibition of *n*-decane for shale samples from the Longmaxi and Wufeng Formations.

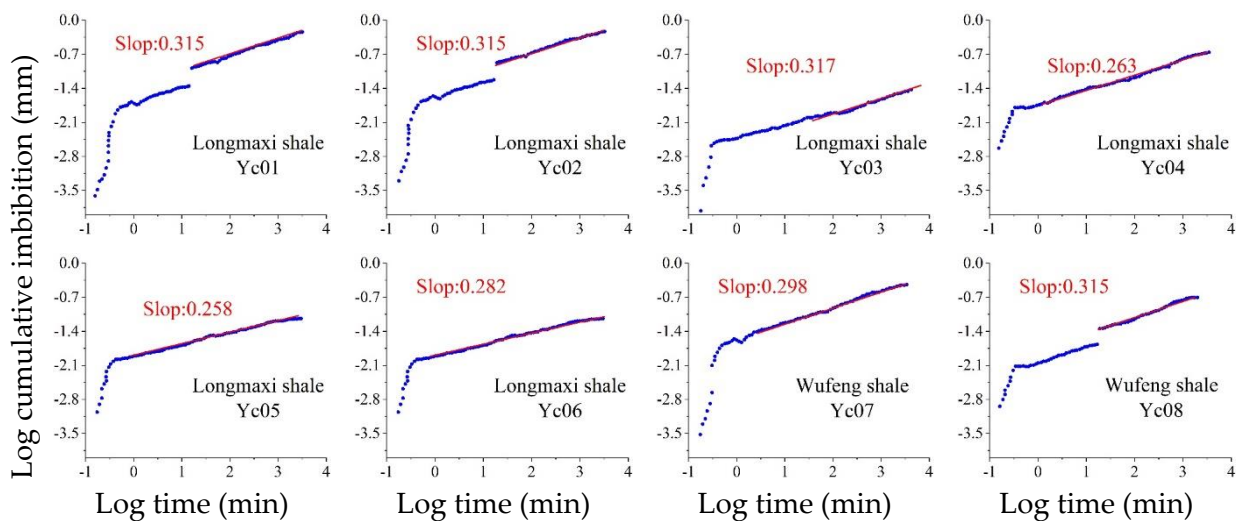


Figure 6. Log plot of the cumulative imbibition of water for shale samples from the Longmaxi and Wufeng Formations.

Table 3. Statistical of slopes of self-absorption curves of deionized water and *n*-decane fluid in Wufeng–Longmaxi Formation in the study area.

Formation		Longmaxi				Wufeng			
Samples		Yc01	Yc02	Yc03	Yc04	Yc05	Yc06	Yc07	Yc08
Self-absorption slop	deionized water	0.3147	0.3147	0.3169	0.2625	0.2576	0.2822	0.2983	0.3153
	<i>n</i> -decane	0.3521	0.4061	0.3408	0.254	0.2775	0.2708	0.4154	0.4281
Hydrophilic pore connectivity		medium	medium	weak	medium	weak	weak	weak	medium
Oilphilic pore connectivity		medium	medium	medium	weak	weak	weak	medium	medium

In the analysis of pore connectivity, the gray absorption coefficient difference of X-rays is frequently used to identify fractures, OM, and matrix minerals such as pyrite. These components are commonly assigned the red, blue, gray, and yellow colors, respectively [39]. This approach was adopted to reconstruct and examine the 3D structural characteristics of the Yc-08 (WF Formation) and Yc-03 (LMX Formation) samples (Figure 7a,b), and

the associated pore structures were highlighted (Figure 7c,d). To characterize the pore connectivity, a pore network model was constructed using a sphere, an orange-red cylinder, and a white cylinder to represent spheres and small, medium, and large throats, respectively (Figure 7e,f). Importantly, X-ray mainly uses the pixel number to distinguish the size of the material composition. The connected small pixels are identified as a large set of pixels. Therefore, the connected pores will be identified as macropore aggregates. This technology has been applied to the study of WF-LMX Formation shale in the same basin [24,39].

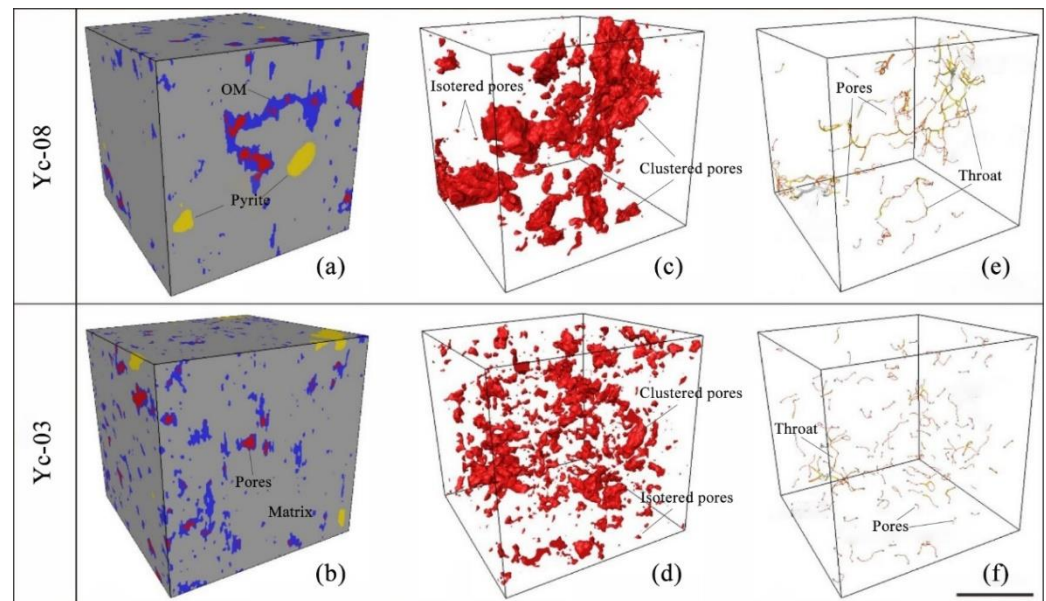


Figure 7. Models from X-ray analysis of samples Yc-08 and Yc-03 demonstrating (a,b) microstructures, (c,d) pores, and (e,f) pore connectivity characteristics under skeleton model. Organic matter is represented by OM, while the horizontal black line in the bottom right corner is set to a scale of 10 μm .

In general, pores in the shale from the WF Formation were characterized by good connectivity, and this is consistent with results from the spontaneous absorption experiments (Figure 7e). Conversely, pores in the sample from the LMX Formation shale were mostly flat, discrete, and dispersed in 3D. In fact, adjacent pores in the sample were commonly connected by just one small throat. The connected pore throat system is limited due to its poor connectivity (Figure 7f).

5. Discussion

5.1. Effects of Samples Size on Pore Connectivity

Both the contact area of the bottom surface and the length of samples used for testing can affect the imbibition and pore connectivity evaluation results [40,41]. In the present study, to evaluate the influence of the bottom surface and length of sample on the imbibition results, two groups of *n*-decane imbibition experiments were conducted, and the results are displayed in Figure 8. In the first group, the test samples measured 10 and 18 mm in diameter and 20 mm in length, while the second group comprised samples with lengths of 10 and 15 mm, and a diameter of 15 mm.

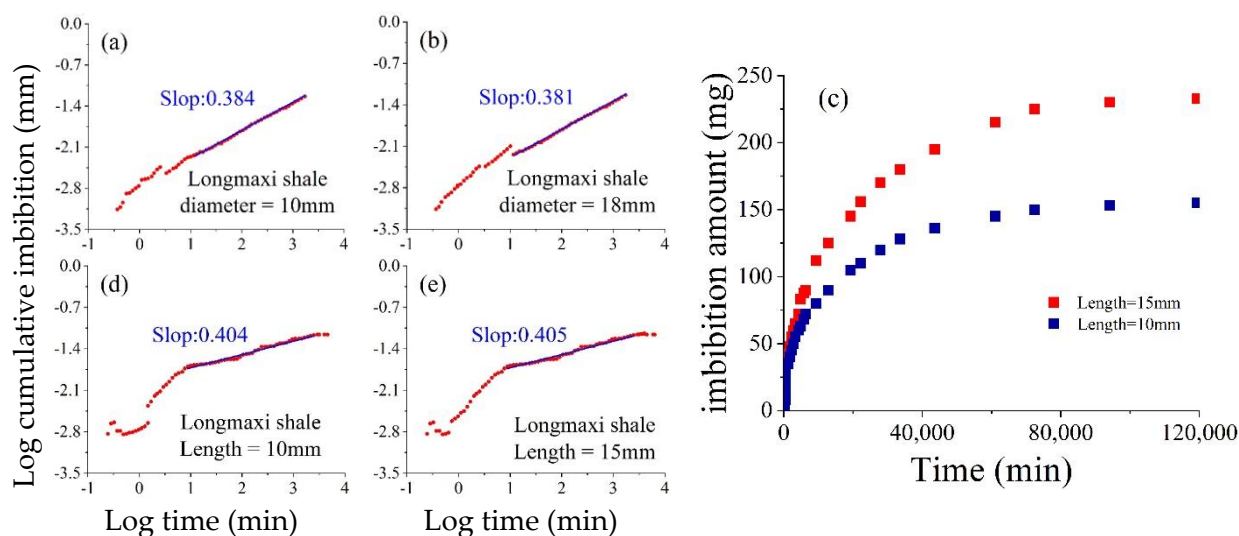


Figure 8. Log cumulative water imbibition versus log imbibition time for the different diameter and length shale samples. Samples of (a) 10 mm and (b) 18 mm in diameter for cumulative imbibition. Samples of (c) 10 mm and 15 mm in length for imbibition amount. Samples of (d) 10 mm and (e) 15 mm in length for cumulative imbibition.

The imbibition curves for samples with varying bottom surface diameters differed, but changes during the imbibition were comparable. Imbibition ended after similar durations and the slopes of swelling (approximately 0.38 in Figure 8a,b) were comparable. These characteristics highlight a minor influence of the diameter of the bottom surface on the imbibition behavior of a sample. In addition, the pore throat structures of samples obtained from nearly identical positions exhibited similarities.

The imbibition curves of samples with varying lengths were similar, but differences emerged in the imbibition volume. The imbibition amount and the time required to attain imbibition equilibrium increased according to the length of the samples (Figure 8c). However, samples with different lengths produced comparable slopes of swelling (approximately 0.40 in Figure 8d,e). These results indicate that heterogeneity in the shales was inconspicuous at the scale of the experiments, and their lipophilic pores exhibited higher connectivity values relative to the hydrophilic pores. These observations are consistent with imbibition results reported for shales from other areas [41–43].

5.2. Contributions of Pore Types to Connectivity

In nature, pore types in shales, such as OM, microfractures, intergranular (InterP), and intragranular (IntraP), display varying distribution characteristics, and these largely determine the degree of pore connectivity [44,45]. The development of pores in OM often affects the pore connectivity in shales in OM-rich shales because during diagenesis, the InterP and IntraP associated with both ductile and rigid minerals are significantly reduced through compaction. Microfractures and macropores related to quartz and clay minerals are also diminished via compaction as the burial depth increases. Alternatively, micro- and meso-scale pores in OM eventually become the dominant type in OM-rich shales beyond the diagenesis stage, while other pore types and sizes are eliminated [46]. According to results of the low-pressure N₂ adsorption and high-pressure Hg injection experiments, pores in OM and residual micro-mesopores are the dominant types in shales from the study area.

The results of the imbibition experiments and X-ray tests revealed that the pore connectivity values for shales from the WF Formation were higher than those for shales from the LMX Formation. In addition, the number of oil-wet pores was slightly higher than the number of water-wet pores in samples from both formations. These differences are attributed to the OM content of the samples and the types of pores preserved. The

higher contents of OM and brittle minerals, such as silica in the shales of the WF Formation, favored the preservation of OM and intergranular pores as well as the development of microfractures, and this promoted connectivity between different pore types (Figure 7c,e). In contrast, the low contents of OM and brittle minerals in the shales of the LMX Formation limited the development of intergranular pores and microfractures, and thus, the samples were characterized by weak pore connectivity (Figure 7d,f).

The contribution of OM pores to the pore connectivity in shales can be evaluated using the following equations:

$$\Phi_{OM} = \Phi_S V_{OM} / V_{shale} = \Phi_S w_{OM} \rho_{shale} / \rho_{OM}$$

where Φ_{OM} and Φ_S represent the OM porosity and OM surface porosity, respectively; w_{OM} is the mass fraction of OM; ρ_{shale} and ρ_{OM} denote the density of shale (2.60 g/cm³) and OM (1.29 g/cm³), respectively [46]. Based on the SEM images (Figure 9), Φ_S values were calculated for the samples studied using the JMicrovision software, and the average value of Φ_S was 18.75% (for WF Formation) and 17.96% (for the LMX Formation), respectively (Table 4). According to the calculations, the average Φ_{OM} for the shales of the WF and LMX Formation were 1.73% and 0.41%, and these accounted for 89.4% and 24.7% of the corresponding total porosity, respectively. Evidently, a higher OM content promotes pore connectivity in shales; that is, the presence of OM pores is conducive to the enhancement of pore connectivity in shales.

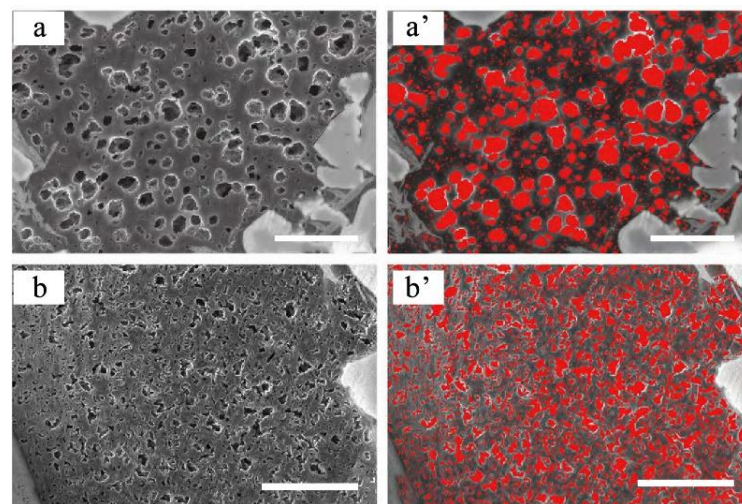


Figure 9. SEM images utilized for calculation of pores associated with organic matter in shales from the WF-LMX Formation. The left graph is the original SEM for the (a) WF Formation and (b) LMX Formation, and the right graph is the software to delineate the pore image for the (a') WF Formation and (b') LMX Formation, respectively.

Table 4. Results of the surface organic matter porosities (Φ_S , %).

No.	Φ_S (%)	No.	Φ_S (%)	No.	Φ_S (%)	No.	Φ_S (%)	No.	Φ_S (%)
LMX01	7.96	LMX10	12.67	LMX19	18.14	WF01	21.45	WF10	36.79
LMX02	11.35	LMX11	19.44	LMX20	18.45	WF02	17.44	WF11	11.55
LMX03	17.66	LMX12	21.22	LMX21	20.54	WF03	16.98	WF12	17.99
LMX04	18.13	LMX13	18.46	LMX22	22.36	WF04	15.13	WF13	20.06
LMX05	19.24	LMX14	18.81	LMX23	24.78	WF05	17.99	WF14	17.32
LMX06	8.96	LMX15	14.31	LMX24	31.05	WF06	19.35	WF15	18.66
LMX07	9.17	LMX16	19.77	LMX25	22.07	WF07	17.95	WF16	17.89
LMX08	12.55	LMX17	18.99	LMX26	19.14	WF08	16.36	WF17	18.35
LMX09	21.05	LMX18	19.54	LMX27	19.12	WF09	18.92	WF18	17.33
Average			17.96			Average			18.75

5.3. Contribution of Different Pore Sizes to the Connectivity

Both the pore types and size affect the connectivity of pores in shales. The influence of macropores and micropores on fluid flow in rocks has often been debated. However, the initial entry of fluids into pores is controlled by capillary pressure and friction [47].

Wang et al. [42] used nuclear magnetic resonance (NMR) to study the imbibition behavior of different pores in shales from the Shahejie Formation and reported that pore connectivity was mainly controlled by micropores. Meng et al. [48] used shales from the LMX Formation to demonstrate that deionized water preferentially permeated the samples through micropores during imbibition experiments. In a study of shales from the WF-LMX Formation in the Fuling area, Yang et al. [49] indicated that the presence of micropores and mesopores promoted the connectivity of pores. Thus, the proportion of micropores in shales is evidently a major control on the connectivity of pores.

In the present study, shales from the WF-LMX Formation were rich in nano- to micro-scale OM particles that were disseminated among clastic particles. The OM particles contained numerous secondary pores that were developed during catagenesis. Evidently, the SEM images in Figure 9 reveal numerous secondary pores characterized by small throat sizes within the OM particles. These can produce good networks of OM pores within the shales, and thus enhance the connectivity of pores.

5.4. Factors Influencing Pore Connectivity in the Shales

Pore types in organic matter-rich shales are complex and diverse, and the characteristics of their development and connectivity are often controlled by external and internal factors. External control factors include tectonic stress and sedimentary environment, and internal control factors are associated with the morphology of particles, temperature, stress, OM content, mineral composition, and OM maturity [36,42]. The triaxial stress physical experiment of organic-rich shale in other sections of the same basin found that when the confining pressure of shale samples was less than 16.6 MPa, many microcracks began to occur in the shale, indicating that the generation of microcracks in shale was closely related to the stress conditions of the formation [50]. It is worth noting that before the uplift of Mesozoic strata, the marine strata in the study area experienced a long period of continuous subsidence. Subsequently, the strata were greatly uplifted due to structural changes, and the formation temperature was reduced. The number of secondary organic pores closely related to the generation and expulsion of organic matter no longer increased. The strata of the WF-LMX Formation in the study area experienced similar structural changes, and the influence of stress changes is not further discussed in this work. The OM particles in shales of the WF-LMX Formation have attained the overmature stage of thermal evolution [34]. The subsequent discussion of the total porosity, effective porosity, and pore connectivity in the shales focuses on the TOC content and mineral composition.

5.4.1. TOC Contents

The TOC content of the shales from the WF-LMX Formation displayed strong positive correlations with the specific surface area associated with micropores and BET specific surface area (Figure 10a,d). These results indicate that numerous micropores were formed in the shales of the WF-LMX Formation during hydrocarbon generation and expulsion. Therefore, complex micropore-dominated networks were created in these shales. The nanoscale pores provided abundant sites for adsorption, and these enhanced the specific surface areas and the adsorption capacities of the shales. In addition, as the TOC content of the samples increased, the total porosity did not undergo a major change (Table 3). These results further demonstrate that shales in the WF-LMX Formation are dominated by secondary micropores and mesopores in the OM. Conversely, macropores, which are commonly associated with the inorganic components, are scarce.

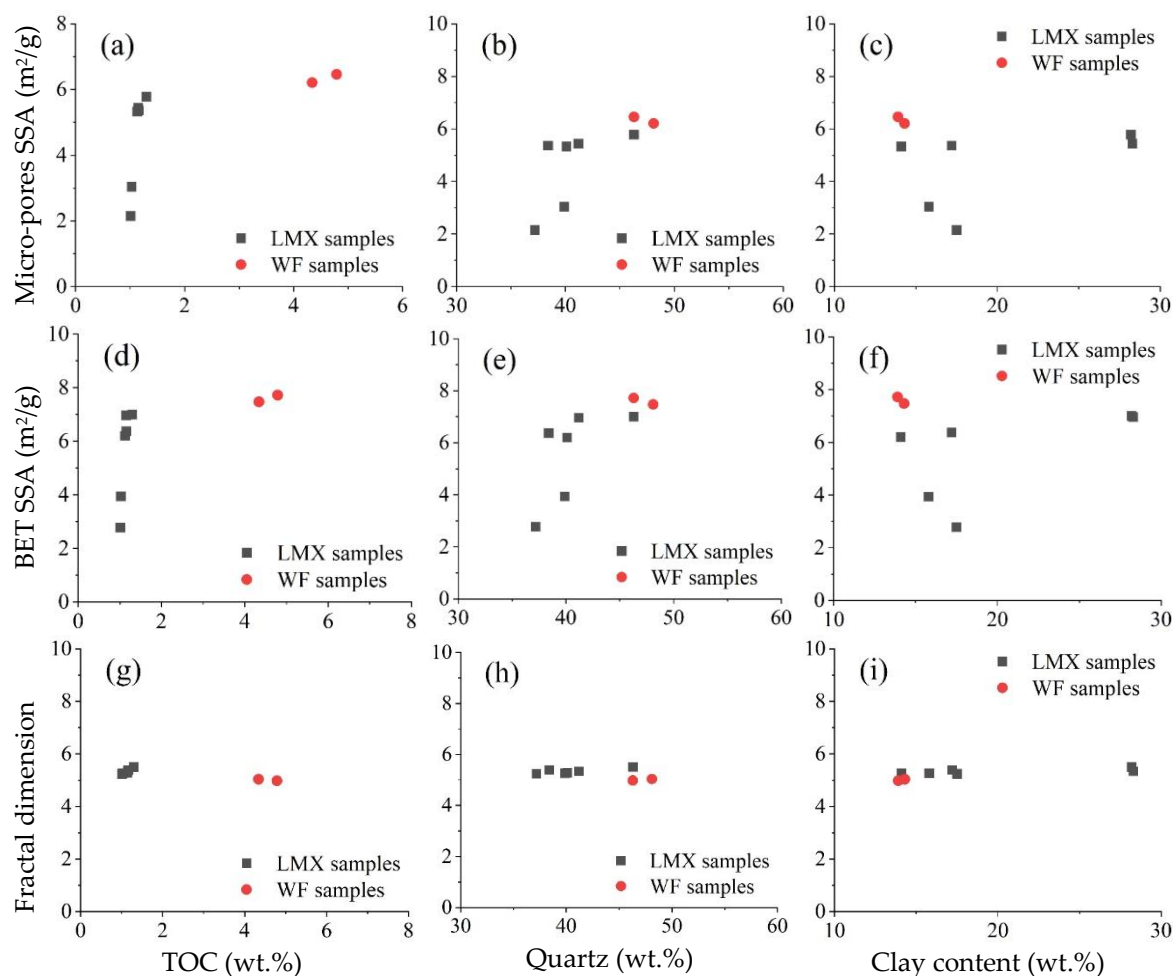


Figure 10. Relationships between shale pore structure parameters and TOC (a,d,g), quartz (b,e,h), and clay minerals (c,f,i).

The variation of the average pore throat size versus the TOC content of shales from the WF-LMX Formation initially decreased, and then increased (Table 2, not shown), while the fractal dimension exhibited a trend of first increasing and then decreasing (Figure 10g). These results also indicate that micropores are abundant in the shales studied. In addition, macropores are transformed into micropores by compression associated with overlying strata, and this can elevate the roughness of surfaces of pores in shales. Accordingly, the fractal dimensions of shales are also increased. In contrast, micropores and mesopores in shales are relatively shielded from compaction, and the presence of fluids in these nanoscale pores commonly generates overpressure. This explains the round or oval shape of most pores observed in the shales from the WF-LMX Formation [51]. The increase in compaction led to the decrease in mineral pore space, particularly the decrease in interP or intraP of clay minerals, which is conducive to enhancing the homogeneity of pores. A weak positive correlation was also observed between the osmotic slope and the TOC content of the samples (Table 2, not shown), and this further indicates that an increase in the OM content of the shales improved the connectivity of pores.

5.4.2. Mineral Compositions

Shales contain diverse minerals that are associated with different specific surface areas. Owing to differences in the composition of minerals, the pore structure characteristics of the shales obviously differ. In the black shale from the WF-LMX Formation, despite the complex composition, quartz and clay minerals (illite, chlorite, and illite-montmorillonite mixed layer) dominated, followed by minor amounts of feldspars, carbonates, pyrite, hematite,

etc. The quartz and clay mineral contents correspondingly increased and decreased with depth, but these accounted for more than 50% of minerals in all samples studied (Table 1 and Figure 2). Therefore, the proportions of these minerals in the samples significantly influenced the associated pore structures.

The micropore-specific surface area, BET-specific surface area, and fractal dimension of shales from the WF-LMX Formation increased as the quartz content increased (Figure 10b,e,h). Considering that the total porosity is controlled by several factors, the correlation between the total porosity and the quartz content was weak (Table 2). Owing to its brittle characteristic, quartz underwent some dissolution during the thermal evolution involving petroleum generation and expulsion from OM. This produced dissolved particles associated with the interP or intraP, and thus, porosity elevated. This also enhanced the reservoir and percolation capacity of shales in the WF-LMX Formation.

The degree of pore development associated with clay minerals depends on the type, relative proportion, structural water content, thermal evolution, and extent of crystallization. In contrast to variations of quartz relative to pore structure parameters, the clay mineral content displayed negative correlations with the micropore- and BET-specific surface areas (Figure 10c,f). A rock with a high clay mineral and a low rigid mineral (e.g., quartz, feldspars, pyrite, and carbonates) content is characterized by strong plasticity and low mechanical strength. Mechanical compaction caused by overlying strata destroys pores, thereby reducing porosity [52]. In addition, due to variations in the types of pores linked to clay minerals and the secondary pores in OM in the shales, correlations between the clay mineral content, average pore size, and fractal dimension were also weak (Table 2, not shown). The reason for this phenomenon is mainly related to the secondary nanoscale organic matter pores developed in shale with a relatively large pore size range.

6. Conclusions

The findings of the present study are summarized as follows: (1) the WF-LMX Formation shale mainly developed micropores and mesopores with pore sizes of 2~6 nm. (2) The oil-wetting of the pores was relatively stronger than the water-wetting, and the pore connectivity of the WF Formation was better than that of the LMX Formation. (3) The increase in the content of brittle minerals, such as TOC and quartz, promoted the development of secondary pores, increased the proportion of micropores and mesopores in total pores, and promoted the connectivity between pores in geological stress and thermal evolution. This work mainly used qualitative and quantitative methods to evaluate shale pore characteristics, and analyzed the main influencing factors for shale pore connectivity, which can provide theoretical guidance for improving shale gas production.

Author Contributions: Investigation, F.Z. and Z.D.; methodology, Z.D. and C.W.; data curation, W.Z. and R.Y.; writing—original draft, F.Z. All authors have read and agreed to the published version of the manuscript.

Funding: This study was funded by the National Natural Science Foundation of China (No. 41772129).

Institutional Review Board Statement: Not applicable.

Informed Consent Statement: Not applicable.

Data Availability Statement: Not applicable.

Conflicts of Interest: The authors declared no potential conflicts of interest with respect to the research, authorship, and/or publication of this article.

References

1. Ma, X.; Wang, H.; Zhou, S.; Feng, Z.; Liu, H.; Guo, W. Insights into NMR response characteristics of shales and its application in shale gas reservoir evaluation. *J. Nat. Gas. Sci. Eng.* **2020**, *84*, 103674. [[CrossRef](#)]
2. Feng, Z.; Hao, F.; Dong, D.; Zhou, S.; Wu, W.; Xie, C.; Cai, Y.; Li, Z. Geochemical anomalies in the Lower Silurian shale gas from the Sichuan Basin, China: Insights from a Rayleigh-type fractionation model. *Org. Geochem.* **2020**, *142*, 103981. [[CrossRef](#)]

3. Hao, F.; Zou, H.; Lu, Y. Mechanisms of shale gas storage: Implications for shale gas exploration in China. *AAPG Bull.* **2013**, *97*, 1325–1346. [[CrossRef](#)]
4. Hao, F.; Zou, H. Cause of shale gas geochemical anomalies and mechanisms for gas enrichment and depletion in high-maturity shales. *Mar. Pet. Geol.* **2013**, *44*, 1–12. [[CrossRef](#)]
5. Curtis, J.B. Fractured shale-gas systems. *AAPG Bull.* **2002**, *86*, 1921–1938.
6. Ross, D.J.K.; Bustin, R.M. The importance of shale composition and pore structure upon gas storage potential of shale gas reservoirs. *Mar. Pet. Geol.* **2009**, *26*, 916–927. [[CrossRef](#)]
7. Zou, C.; Yang, Z.; Pan, S.; Chen, Y.; Lin, S.; Huang, J.; Wu, S.; Dong, D.; Wang, S.; Liang, F.; et al. Shale Gas Formation and Occurrence in China: An Overview of the Current Status and Future Potential. *Acta. Geol. Sin-Engl.* **2016**, *90*, 1249–1283.
8. Chen, C.; Hu, D.; Westacott, D.; Loveless, D. Nanometer-scale characterization of microscopic pores in shale kerogen by image analysis and pore-scale modeling. *Geochem. Geophys. Geosystems* **2013**, *14*, 4066–4075. [[CrossRef](#)]
9. Chen, L.; Zhang, L.; Kang, Q.; Viswanathan, H.S.; Yao, J.; Tao, W. Nanoscale simulation of shale transport properties using the lattice Boltzmann method: Permeability and diffusivity. *Sci. Rep.* **2015**, *5*, 8089. [[CrossRef](#)]
10. Chen, L.; Kang, Q.; Pawar, R.; He, Y.; Tao, W. Pore-scale prediction of transport properties in reconstructed nanostructures of organic matter in shales. *Fuel* **2015**, *158*, 650–658. [[CrossRef](#)]
11. Yuan, Y.; Rezaee, R.; Verrall, M.; Hu, S.; Zou, J.; Testmanti, N. Pore characterization and clay bound water assessment in shale with a combination of NMR and low-pressure nitrogen gas adsorption. *Int. J. Coal. Geol.* **2018**, *194*, 11–21. [[CrossRef](#)]
12. Zhang, W.; Huang, Z.; Li, X.; Chen, J.; Guo, X.; Pan, Y.; Liu, B. Estimation of organic and inorganic porosity in shale by NMR method, insights from marine shales with different maturities. *J. Nat. Gas. Sci. Eng.* **2020**, *78*, 103290. [[CrossRef](#)]
13. Garcia, A.P.; Han, Y.; Heidari, Z. Integrated Workflow to Estimate Permeability Through Quantification of Rock Fabric Using Joint Interpretation of Nuclear Magnetic Resonance and Electric Measurements. *Petrophysics* **2018**, *59*, 672–693.
14. Tathed, P.; Han, Y.; Misra, S. Hydrocarbon saturation in Bakken Petroleum System based on joint inversion of resistivity and dielectric dispersion logs. *Fuel* **2018**, *233*, 45–55. [[CrossRef](#)]
15. Han, Y.; Misra, S. Joint petrophysical inversion of multifrequency conductivity and permittivity logs derived from subsurface galvanic, induction, propagation, and dielectric dispersion measurements. *Geophysics* **2018**, *83*, D97–D112. [[CrossRef](#)]
16. Han, Y.; Misra, S. Bakken Petroleum System Characterization Using Dielectric-Dispersion Logs. *Petrophysics* **2018**, *59*, 201–217. [[CrossRef](#)]
17. Ma, Y.; Pan, Z.; Zhong, N.; Connell, L.D.; Down, D.I.; Lin, W.; Zhang, Y. Experimental study of anisotropic gas permeability and its relationship with fracture structure of Longmaxi Shales, Sichuan Basin, China. *Fuel* **2016**, *180*, 106–115. [[CrossRef](#)]
18. Wang, X.; Hou, J.; Li, S.; Dou, L.; Song, S.; Kang, Q.; Wang, D. Insight into the nanoscale pore structure of organic-matter shales in the Bakken Formation, USA. *J. Petrol. Sci. Eng.* **2020**, *191*, 107182. [[CrossRef](#)]
19. Wu, J.; Yuan, Y.; Niu, S.; Wei, X.; Yang, J. Multiscale characterization of pore structure and connectivity of Wufeng-Longmaxi shale in Sichuan Basin, China. *Mar. Pet. Geol.* **2020**, *120*, 104514. [[CrossRef](#)]
20. Sun, M.; Yu, B.; Hu, Q.; Zhang, Y.; Li, B.; Yang, R.; Melnichenko, Y.B.; Cheng, G. Pore characteristics of Longmaxi shale gas reservoir in the Northwest of Guizhou, China: Investigations using small-angle neutron scattering (SANS), helium pycnometry, and gas sorption isotherm. *Int. J. Coal. Geol.* **2017**, *171*, 61–68. [[CrossRef](#)]
21. Gu, X.; Mildner, D.F.R.; Cole, D.R.; Rother, G.; Slingerland, R.; Brantley, S.L. Quantification of Organic Porosity and Water Accessibility in Marcellus Shale Using Neutron Scattering. *Energy Fuels* **2016**, *30*, 4438–4449. [[CrossRef](#)]
22. Klaver, J.; Hemes, S.; Houben, M.; Desbois, G.; Radi, Z.; Urai, J.L. The connectivity of pore space in mudstones: Insights from high-pressure Wood's metal injection, BIB-SEM imaging, and mercury intrusion porosimetry. *Geofluids* **2015**, *15*, 577–591. [[CrossRef](#)]
23. Wang, Y.; Pu, J.; Wang, L.; Wang, J.; Jiang, Z.; Song, Y.; Wang, C.; Wang, Y.; Jin, C. Characterization of typical 3D pore networks of Jiulaodong formation shale using nano-transmission X-ray microscopy. *Fuel* **2016**, *170*, 84–91. [[CrossRef](#)]
24. Tang, X.; Jiang, Z.; Jiang, S.; Li, Z. Heterogeneous nanoporosity of the Silurian Longmaxi Formation shale gas reservoir in the Sichuan Basin using the QEMSCAN, FIB-SEM, and nano-CT methods. *Mar. Pet. Geol.* **2016**, *78*, 99–109. [[CrossRef](#)]
25. Hu, Q.; Ewing, R.P.; Dultz, S. Low pore connectivity in natural rock. *J. Contam. Hydrol.* **2012**, *133*, 76–83. [[CrossRef](#)] [[PubMed](#)]
26. Zhang, C.; Santosh, M.; Zhu, Q.; Chen, X.; Huang, W. The Gondwana connection of South China: Evidence from monazite and zircon geochronology in the Cathaysia Block. *Gondwana Res.* **2015**, *28*, 1137–1151. [[CrossRef](#)]
27. Chen, X.; Rong, J.; Li, Y.; Boucot, A.J. Facies patterns and geography of the Yangtze region, South China, through the Ordovician and Silurian transition. *Palaeogeogr. Palaeoclimatol. Palaeoecol.* **2004**, *204*, 353–372.
28. Wang, C.; Dong, Z.; Fu, X.; Chen, Q.; Liu, X.; Tang, M.; Wang, Z. Spatiotemporal Evolution and Genesis of the Late Ordovician-Early Silurian Marine Euxinia in Northeastern Upper Yangtze Basin, South China. *Front. Earth Sci.* **2021**, *9*, 1–19. [[CrossRef](#)]
29. Bakshi, T.; Prusty, B.K.; Pathak, K.; Pal, S.K. Pore characteristics of Damodar valley shale and their effect on gas storage potential. *J. Pet. Sci. Eng.* **2018**, *162*, 725–735. [[CrossRef](#)]
30. Barrett, P.E.; Joyner, G.L.; Halenda, P.P. The Determination of Pore Volume and Area Distributions in Porous Substances. I. Computations from Nitrogen Isotherms. *J. Am. Chem. Soc.* **1951**, *73*, 373–380. [[CrossRef](#)]
31. Avnir, D.; Jaroniec, M. An Isotherm Equation for Adsorption on Fractal Surfaces of Heterogeneous Porous Materials. *Langmuir* **1989**, *5*, 1431–1433. [[CrossRef](#)]
32. Washburn, W.E. The dynamics of capillary flow. *Phys. Rev.* **1921**, *17*, 273–283. [[CrossRef](#)]

33. Peng, S.; Zhang, T.; Loucks, R.G.; Shultz, J. Application of mercury injection capillary pressure to mudrocks: Conformance and compression corrections. *Mar. Pet. Geol.* **2017**, *88*, 30–40. [[CrossRef](#)]
34. Wang, C.; Dong, Z.; Fu, X.; Hu, X.; Li, Z. Origin and paleoenvironment of organic matter in the Wufeng–Longmaxi shales in the northeastern Sichuan basin. *Energy Explor. Exploit.* **2021**, *39*, 134–155. [[CrossRef](#)]
35. Yu, L.; Liu, K.; Fan, M.; Pan, Z. Pore Connectivity Characterization Using Coupled Wood’s Metal Intrusion and High-Resolution Imaging: A Case of the Silurian Longmaxi Shales From the Sichuan Basin, China. *Front. Earth Sci.* **2021**, *9*, 1–16. [[CrossRef](#)]
36. Mason, G.; Fischer, H.; Morrow, N.R.; Ruth, D.W.; Wo, S. Effect of sample shape on counter-current spontaneous imbibition production vs time curves. *J. Petrol. Sci. Eng.* **2009**, *66*, 83–97. [[CrossRef](#)]
37. Yang, H.; Zhang, B.; Yang, K.; Xiao, W.; Wang, Y. The study on shale electrical properties based on characterization of microscopic pore structure: A case study of Longmaxi formation shale in south Sichuan. *Comput. Tech. Geophys. Geochem. Explor.* **2021**, *43*, 646–654.
38. Yang, R. Pore Structure and Tracer-Containing Fluid Migration in Connected Pores of Wufeng and Longmaxi Shales from Western Hubie and Eastern Chongqing Regions. Ph.D. Thesis, China University of Geosciences, Wuhan, China, 2018.
39. Gou, Q.; Xu, S.; Hao, F.; Shu, Z.; He, S.; Wu, Z. Differences in the Nanopore Structure of Organic-Rich Shales with Distinct Sedimentary Environments and Mineral Compositions. *Energy Fuels* **2021**, *35*, 16562–16577. [[CrossRef](#)]
40. Wang, X.; Zhang, F.; Li, S.; Dou, L.; Liu, Y.; Ren, X.; Chen, D.; Zhao, W. The Architectural Surfaces Characteristics of Sandy Braided River Reservoirs, Case Study in Gudong Oil Field, China. *Geofluids* **2021**, *2021*, 8821711. [[CrossRef](#)]
41. Hatiboglu, C.U.; Babadagli, T. Oil recovery by counter-current spontaneous imbibition: Effects of matrix shape factor, gravity, IFT, oil viscosity, wettability, and rock type. *J. Pet. Sci. Eng.* **2007**, *59*, 106–122. [[CrossRef](#)]
42. Wang, X.; Wang, M.; Li, Y.; Zhang, J.; Li, M.; Li, Z.; Guo, Z.; Li, J. Shale pore connectivity and influencing factors based on spontaneous imbibition combined with a nuclear magnetic resonance experiment. *Mar. Pet. Geol.* **2021**, *132*, 105239. [[CrossRef](#)]
43. Yang, R.; Hu, Q.; Yi, J.; Zhang, B.; He, S.; Guo, X.; Hou, Y.; Dong, T. The effects of mineral composition, TOC content and pore structure on spontaneous imbibition in Lower Jurassic Dongyuemiao shale reservoirs. *Mar. Pet. Geol.* **2019**, *109*, 268–278. [[CrossRef](#)]
44. Loucks, R.G.; Reed, R.M.; Ruppel, S.C.; Hammes, U. Spectrum of pore types and networks in mudrocks and a descriptive classification for matrix-related mudrock pores. *AAPG Bull.* **2012**, *96*, 1071–1098. [[CrossRef](#)]
45. Milliken, K.L.; Rudnicki, M.; Awwiller, D.N.; Zhang, T. Organic matter-hosted pore system, Marcellus Formation (Devonian), Pennsylvania. *AAPG Bull.* **2013**, *97*, 177–200. [[CrossRef](#)]
46. Shi, M.; Yu, B.; Zhang, J.; Huang, H.; Yuan, Y.; Li, B. Microstructural characterization of pores in marine shales of the Lower Silurian Longmaxi Formation, southeastern Sichuan Basin, China. *Mar. Pet. Geol.* **2018**, *94*, 166–178. [[CrossRef](#)]
47. Singh, H. A critical review of water uptake by shales. *J. Nat. Gas Sci. Eng.* **2016**, *34*, 751–766. [[CrossRef](#)]
48. Meng, M.; Ge, H.; Ji, W.; Shen, Y.; Su, S. Monitor the process of shale spontaneous imbibition in co-current and counter-current displacing gas by using low field nuclear magnetic resonance method. *J. Nat. Gas Sci. Eng.* **2015**, *27*, 336–345. [[CrossRef](#)]
49. Yang, R.; Hu, Q.; He, S.; Hao, F.; Guo, X.; Yi, J.; Sun, M. Wettability and connectivity of overmature shales in the Fuling gas field, Sichuan Basin (China). *AAPG Bull.* **2019**, *103*, 653–689. [[CrossRef](#)]
50. Yang, R.; He, S.; Hu, Q.; Hu, D.; Yi, J. Geochemical characteristics and origin of natural gas from Wufeng-Longmaxi shales of the Fuling gas field, Sichuan Basin (China). *Int. J. Coal Geol.* **2017**, *171*, 1–11. [[CrossRef](#)]
51. Pan, J.; Ge, T.; Liu, W.; Wang, K.; Wang, X.; Mou, P.; Wu, W.; Niu, Y. Organic matter provenance and accumulation of transitional facies coal and mudstone in Yangquan, China: Insights from petrology and geochemistry. *J. Nat. Gas. Sci. Eng.* **2021**, *94*, 104076. [[CrossRef](#)]
52. Wang, X.; Liu, Y.; Hou, J.; Li, S.; Kang, Q.; Sun, S.; Ji, L.; Sun, J.; Ma, R. The relationship between synsedimentary fault activity and reservoir quality—A case study of the Ek1 formation in the Wang Guantun area, China. *Interpretation* **2020**, *8*, SM15–SM24. [[CrossRef](#)]